Laser powder bed fusion in situ alloying of AISI 316L-2.5%Cu alloy: microstructure and mechanical properties evolution

Progress in Additive Manufacturing
https://doi.org/10.1007/s40964-023-00557-x

FULL RESEARCH ARTICLE

Laser powder bed fusion in situ alloying of AISI 316L-2.5%Cu alloy: microstructure and mechanical properties evolution

Amir Behjat[1,2] · Morteza Shamanian[1] · Luca Iuliano[2] · Abdollah Saboori[2]

Received: 5 February 2023 / Accepted: 4 December 2023

Abstract
This work investigates the effects of copper addition on the microstructure and mechanical properties of AISI 316L austenitic stainless steel fabricated by the laser powder bed fusion (L-PBF) method. The outcomes reveal that the copper atom dissolves into iron and forms a complete austenitic structure under the condition of the L-PBF process. Microstructural observations demonstrate that the microstructure of the new alloy is characterised by columnar grains consisting of finer cellular structures, as compared to the as-built AISI 316L. The appearance of such a finer sub-structure could be originated from the effect of copper on the cooling rate during the L-PBF process. The energy-dispersive X-ray spectroscopy maps indicate that the distribution of copper in the AISI 316L matrix is homogeneous, and no significant segregation of elements in the matrix is revealed. The results of the tensile tests show that the ultimate tensile strength of AISI 316L-Cu alloy is 558 MPa, whereas the yield strength value and the tensile elongation are 510 MPa and 30.4%, respectively. Two mechanisms of solid solution strengthening, and refinement of cell sizes improve the mechanical properties of AISI316L-Cu alloy compared with AISI 316L one. The microscale fractography of the fracture surface shows ductile fracture with massive dimple networks and brittle fracture with a quasi-cleavage plane, which may indicate the melt pool boundary. All these results confirm that the development of new alloys following the in situ alloying approach is economical and reliable.

Keywords Additive manufacturing · Laser powder bed fusion · 316L stainless steel · In situ alloying · Alloy development

1 Introduction

Additive manufacturing (AM) processes, also known as 3D printing, are introduced as innovative technologies to produce complex 3D objects layer-by-layer directly from a digital model [1]. As a result of their advantages, such as high material utilization, the ability to fabricate complex structures, and short manufacturing cycles, they could attract considerable interest from industry and science [2]. In general, direct metal AM processes can be classified into two subcategories: Powder Bed Fusion (PBF) and Directed Energy Deposition (DED). Laser-PBF (L-PBF) is one of the most popular metal AM techniques used to fabricate complex near-shape metallic components [3, 4]. In the L-PBF process, a metal powder layer is irradiated by a high-energy laser (usually Nd: YAG or fiber laser) to fuse the powder layer selectively according to the CAD file and form a solid layer of a certain thickness [5].

One of the main grades of austenitic stainless steel is AISI316L, which is widely used in industry, biomedical and surgical instruments owing to its excellent performance [6–8]. Nowadays, AISI316L is among the most widely researched alloys in the metal AM research field. So far, several studies have been performed on investigating the microstructure, mechanical properties, and corrosion behaviour of this alloy [9–11]. This indicates the enormous interest in developing and characterising AISI316L processed by AM techniques [12].

However, on one hand, one of the key limitations of AISI316L as an implant material is its susceptibility to localised corrosion and inflammation that causes failures of implants for long-term applications inside human physiological conditions [13, 14]. On the other hand, a limited number of alloys are present in the portfolio of AM,

✉ Abdollah Saboori
Abdollah.saboori@polito.it

[1] Department of Materials Engineering, Isfahan University of Technology, Isfahan 84156-83111, Iran

[2] Integrated Additive Manufacturing Center, Department Management and Production Engineering, Politecnico di Torino, Corso Duca Degli Abruzzi 24, 10129 Turin, Italy

Published online: 24 January 2024

and all of the research on successful production of AM is limited to the alloys available on the commercial market. Therefore, it is necessary to develop new alloys based on the AM methods to obtain better performance in a wide range of applications, especially in medical industries [15, 16].

Currently, considerable methods based on the AM, such as in situ alloying and pre-alloying, are becoming a popular strategy to address the above-mentioned issues [15]. Feedstock modification by in situ alloying is done by adding a small fraction of solute metallic element or intermetallic compound into the starting powder of AM fabricated alloys. Several researchers had successfully printed AM components using modified AISI316L feedstock. Ti [17], Ag [18], TiN [19], TiB_2 [20], and CrN [21] have been studied as potential additives to modify AISI316L.

Recently, copper as a candidate element has attracted more and more attention for improving the mechanical properties and corrosion resistance of stainless steel [9, 10, 22]. Moreover, the antibacterial and biocompatibility effects of Cu ions have been reported by several researchers [10, 23].

To date, no more studies have been done concentrating on using L-PBF to build bulk Cu-containing stainless steel. Wang et al. [14] fabricated a low-stiffness porous AISI 316L-4.5Cu by selective laser with similar stiffness (3–20 GPa) with bone to prevent stress shielding. Foadian et al. [24] investigated AISI316L with two amounts of copper content by the L-PBF technique. They found that component density decreased by the addition of 5% copper.

Nonetheless, there is still a lack of comprehensive understanding of the in situ synthesis of Cu-bearing austenite stainless steel fabricated by the L-PBF process. Therefore, this work aims to investigate the microstructures and mechanical properties of the Cu-bearing austenite stainless steel that is produced via the L-BBF process following the in situ alloying approach.

2 Experimental

2.1 Sample preparation

AISI316L stainless steel gas atomized powder, supplied by Oerlikon, and gas atomized copper powder (Sandvik Osprey Ltd.) were used as the feedstock material. Copper and stainless steel powders were mixed using a very low-energy ball mill without using any ball for 16 h. The copper contents in the mixture powder were 2.5 wt%. Figure 1a shows the morphology and corresponding EDS elemental maps of the starting powder mixture. The result of powder distribution shows that the average particle diameter of the blended AISI316 and Cu are 27 µm (d_{10} = 13 µm, d_{50} = 23 µm, d_{90} = 40 µm) and 6.3 µm (d_{10} = 3.1 µm, d_{50} = 5.3 µm, d_{90} = 13.1 µm), respectively. Table 1 shows the chemical composition of the

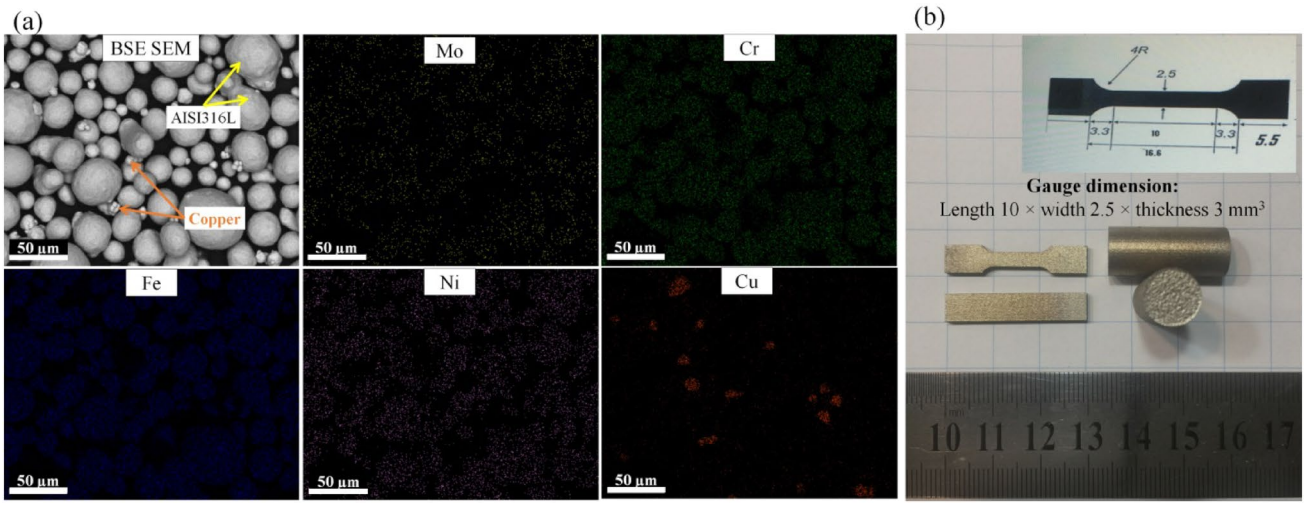

Fig. 1 **a** BSE SEM image of the mixed powder with corresponding EDS elemental maps and **b** representative as-built and machined tensile samples

Table 1 Nominal and analysed chemical composition of mixed AISI316L-Cu powder

Elements	Cr	Ni	Mo	C	Mn	Cu	P	S	Fe
Nominal (wt%)	17–19	13–15	2.25–3	0.03	2.0	2.5	0.025	0.01	Bal
Analysed (wt%)	17.02	13.50	2.04	0.02	2.11	2.92	0.022	0.01	Bal

Cu-containing AISI316L stainless steel powder used in this work analysed by Energy Dispersive X-ray Spectroscopy (EDS).

A Concept Laser MLab CusingR machine equipped with a 100 W fiber laser with 50 µm laser spot size was employed to fabricate the Cu-containing AISI316L samples. Before starting the scanning, the build chamber was evacuated to less than 0.1% residual oxygen content. High-purity Argon was supplied to maintain an inert atmosphere inside the build chamber and reduce the chance of oxidation. Before the sample production, a process parameters optimization procedure was performed following the design of experiment approach to find the best process parameters. The laser power, scan speed, and hatch spacing of 95 W, 500 mm/s, and 84 µm, respectively, were applied for the fabrication of cylindrical bars with a diameter of 10 mm and length of 25 mm and rectangular slab with dimensions of $30 \times 7 \times 3$ mm^3 samples. A bidirectional stripe scanning pattern with a 67° rotation between each successive layer with 25 µm height was used as a scanning strategy. Thereafter, the parts were cut off from the building platform by wire electric discharge machining (EDM). The manufactured samples are shown in Fig. 1b. In addition, to compare, some AISI316L samples were fabricated using the same method and parameters. The relative density of each sample is determined by utilising the Archimedes principle.

2.2 Microstructural analysis

The samples for microstructural examinations were mechanically ground by sandpapers of 180–4000 mesh, followed by polishing with 1 µm diamond paste. After fine polishing, the samples were ultra-sonicated in acetone for 15 min and washed in water. Then, the samples were electrolytically etched in a solution of 65% nitric acid for 20 s at 10 V and washed immediately using alcohol to reveal the austenite microstructure clearly. The microstructure was observed using the Optical Microscope (OM, OlympusGX71) and Scanning Electron Microscope (SEM, Philips, XL30) equipped with EDS. The phase analysis and crystallographic orientations were subsequently investigated on the x–z plane (cross section) of samples using an X-ray diffractometer (XRD, Philips) using Mo Kα X-Ray target (0.7093 Å) at working voltage 40 kV, working current 30 mA, scanning angle range 15°–40° and a step size of 0.02°.

2.3 Mechanical tests

Tensile test samples with gauge dimensions of 10 mm (length) × 2.5 mm (width) × 3 mm (thickness) were prepared from rectangular printed parts. Tensile tests were carried out at a strain rate of 1×10^{-3} s^{-1} on a universal Instron-5982 testing system at room temperature three times for each sample. The fracture surfaces of the tensile samples were analysed using the secondary mode of SEM.

3 Results and discussion

3.1 Microstructure characterisation

Based on the relative density measurement results, AISI316L and AISI316L-Cu samples have a density of 99.8% and 99.2% of the ideal density, respectively. Figure 2 compares the OM micrographs of the as-built AISI316L and AISI316L-Cu samples. As shown in these images, the ring shape melt pools for the as-built AISI316L and AISI316L-Cu samples have an average height of 90 µm and 100 µm and a width of 150 µm and 120 µm, respectively. The difference in melt pool size can be attributed to the rapid solidification and increase in temperature gradient caused by the higher

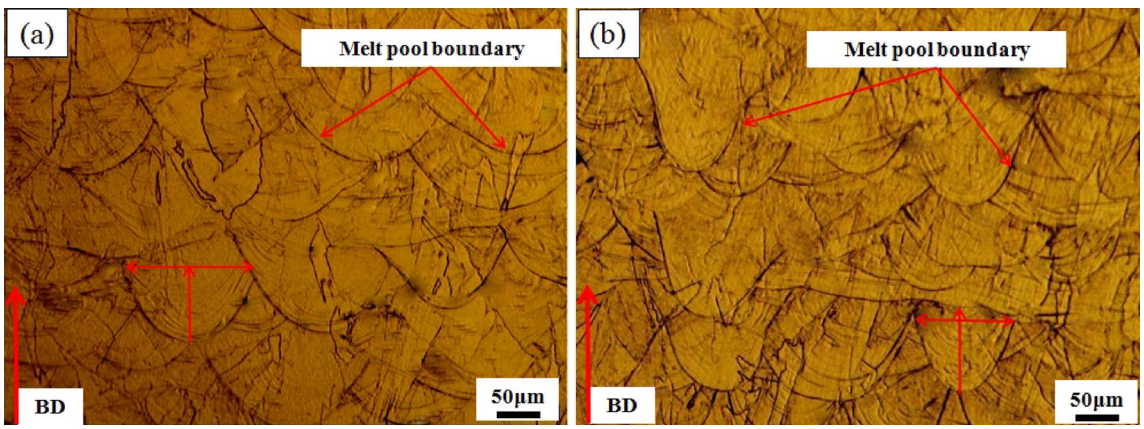

Fig. 2 OM images of the L-PBF-processed as-built **a** AISI316L and **b** AISI316L-Cu

thermal conductivity of pure copper (385 W/m K) compared to stainless steel (10–30 W/m K) [25].

Figure 3a shows the XRD patterns of AISI316L-Cu powders, as-built AISI316L and AISI316L-Cu samples. As can be seen, the strong diffraction peaks corresponding to crystal plane (111), (200), (220), and (311) of Face-Centered Cubic (FCC) austenite (γ phase) are observed in all the samples. In addition, the powder and as-built AISI316L-Cu sample consists of only the FCC phase with no additional peak of ε-Cu phases. This can be related to the resolution of the XRD method that cannot detect the phases in low quantities (typically lower than 3 wt%).

It is well documented that the added copper might be dissolved into iron and form a substitutional solid solution in the steel [9]. Since copper is an austenite stabiliser, it can be expected that the addition of copper leads to the formation of a fully austenitic structure [10]. Moreover, for investigating the effect of Cu on the lattice distortion of AISI316L, the Braggs law is employed to calculate the lattice constants in the XRD patterns. The lattice parameter of the as-built AISI 316L-Cu samples was 0.3601 nm, slightly larger than those of AISI316L (0.3594 nm). Generally, this discrepancy is due to the difference between the radius of the copper atom (0.128 nm) and the iron atom (0.126 nm) [25]. Therefore, this result indicates that the solid solution of copper atoms or substitution of iron atoms by copper causes a slight increase in a lattice distortion of austenite, which is consistent with the results reported by previous works [9, 23].

In addition, it is revealed that changing the solidification mode by adding copper resulted in the crystallite size reduction in the L-PBF copper-bearing AISI316L parts (Fig. 3b). According to previous works [9], increasing the thermal conductivity of material increases the temperature gradient and the cooling rate during solidification. Consequently, the heat extracted from the liquid during dendrite growth increases and results in microstructure refinement. Therefore, According to the Scherrer equation, the relative increase in peak broadening for the AISI316L-Cu sample could result from decreasing the crystallite size.

Figure 4 compares the microstructure of the as-built AISI316L and AISI316L-Cu samples. As can be seen in Fig. 4a, no metallurgical defects, such as pores and cracks, are found in the interface region. As reported in previous works [12], the melt pool dimension depends on the L-PBF process parameters. Moreover, it is revealed that the melt pool tracks have irregular overlaps and fluctuations between adjacent layers.

Figure 4b presents the melt pool solidification, showing both the columnar type of grains and fine cell structures at the micro-level. The appearance of such a sub-structure could be linked to the high cooling rate, extremely complex and non-equilibrium thermal history during the L-PBF process, and a difference in chemical composition due to the low kinetics of homogenisation of bigger atoms [8, 12]. As can be seen, different substructures can be located adjacent to the intersection of several melt track borders. As a result, complex growth orientations of columnar grain perpendicular to the building direction (BD) significantly affect the tensile properties.

The high magnification SEM image (Fig. 4c, d) represents the cell structure with a pentagonal or hexagonal shape formed adjacent to the columnar grain. As can be seen, the cell size of the as-built AISI316L and AISI316L-Cu samples measured using the triangle method [26] are 0.77 ± 0.12 µm

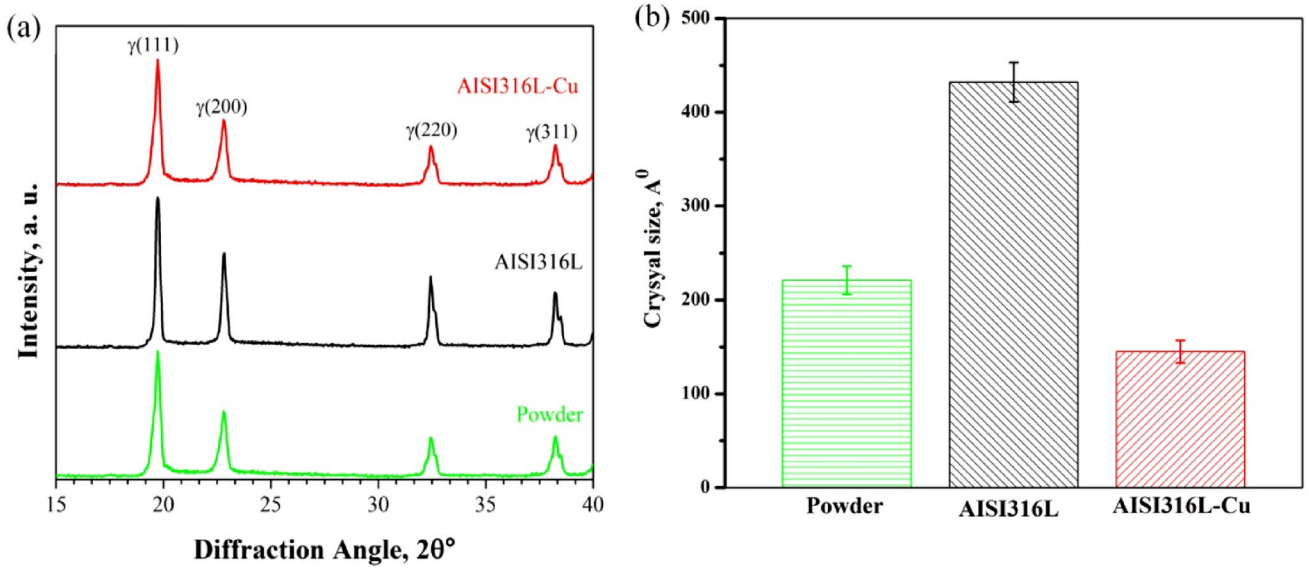

Fig. 3 **a** XRD patterns, and **b** crystallite size of AISI316 L-Cu powder mixture, as-built AISI316L and AISI316L-Cu samples

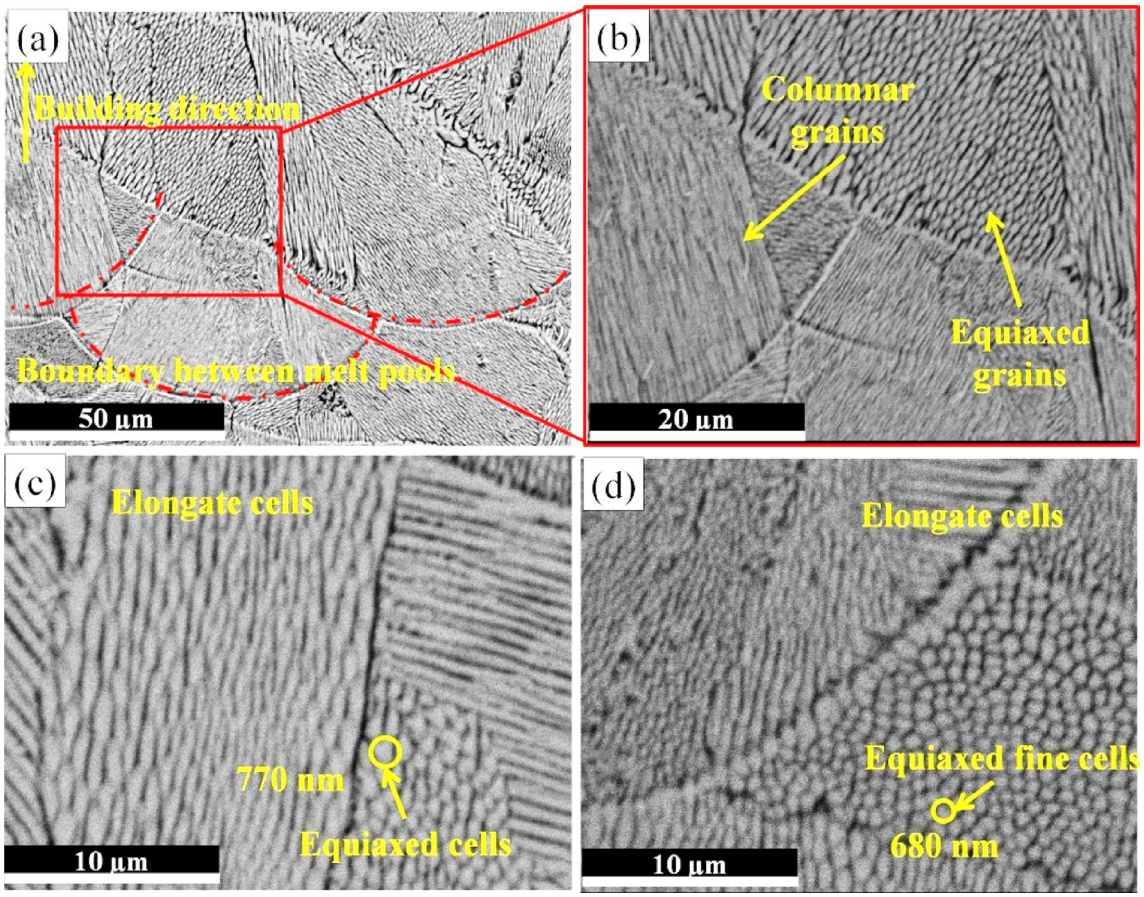

Fig. 4 **a, b** SEM micrograph of the melt pools evolution in as-built AISI316L-Cu sample, cellular structures in **c** as-built AISI316L and **d** as-built AISI316L-Cu

and 0.68 ± 0.17 µm, respectively. The fine cellular microstructures are attributed to the high cooling rate from the resulting local quenching process. As reported by several researchers, the cooling rate during the solidification is the key parameter that has an inverse relationship with the cell size [26]. Therefore, the cooling rates during the solidification for both samples were also estimated. The outcomes of this evaluation indicated that the formation of 0.77 µm and 0.68 µm cells resulted from a cooling rate equal to 1.1×10^6 K/s and 1.8×10^6 K/s for the as-built AISI316L and AISI316L-Cu samples, respectively. Therefore, it could be concluded that the higher thermal conductivity of the new alloy that is achieved through the addition of copper increased the cooling rate during the L-BPF process and, consequently, decreased its cell size. This outcome is in line with the findings of the XRD analysis.

The results of the EDS map analysis that was performed to investigate element distributions across the as-built AISI316L-Cu sample are displayed in Fig. 5. From the EDS maps, it is evident that the sub-structure is rather homogeneous, and no significant segregation of copper was found in the as-built state.

However, it is believed that rapid solidification during the building process, in conjunction with reheating the solidified layers, can promote alloying element segregation and result in microstructure variations. Therefore, the sub-structure appears brighter in the backscattered SEM image (Fig. 6a), which is caused by higher alloy elements and local elemental segregation during the L-PBF process. As can be seen in Fig. 6b, according to EDS point elemental analysis, the intercellular microstructure (spot 1) is richer in nickel and molybdenum and depleted from chromium and copper in comparison with the sub-structure wall/boundary.

3.2 Mechanical properties

Figure 7 compares the room temperature micro tensile responses of the L-PBF AISI316L-Cu and AISI316L along the build direction.

According to the stress–strain curves reported in Fig. 7, the Ultimate Tensile Strength (UTS) of the as-built Cu-AISI316L is 558 MPa, whereas its Yield Stress (YS) and the elongation to fracture (ε_f) are found to be 515 MPa and 30.4%, respectively. Besides, it is found that the UTS, YS,

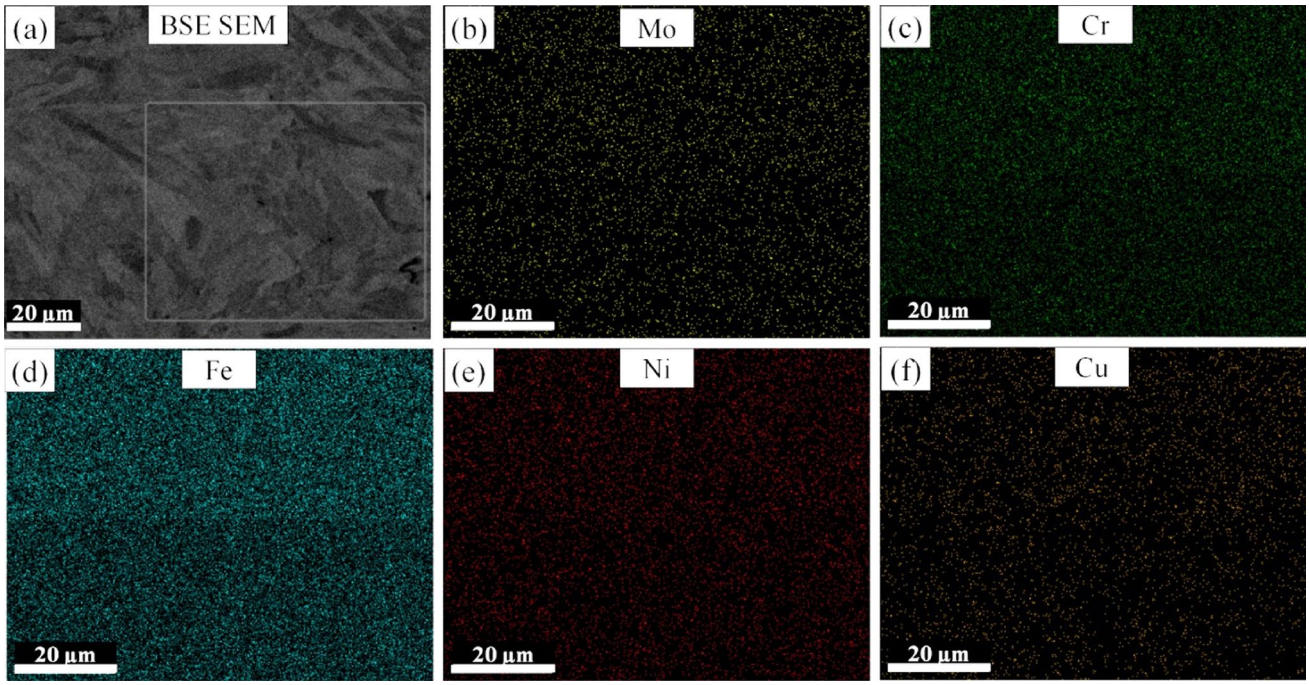

Fig. 5 **a** Backscattered SEM image as-built AISI316L-Cu and **b–f** corresponding EDS elemental maps

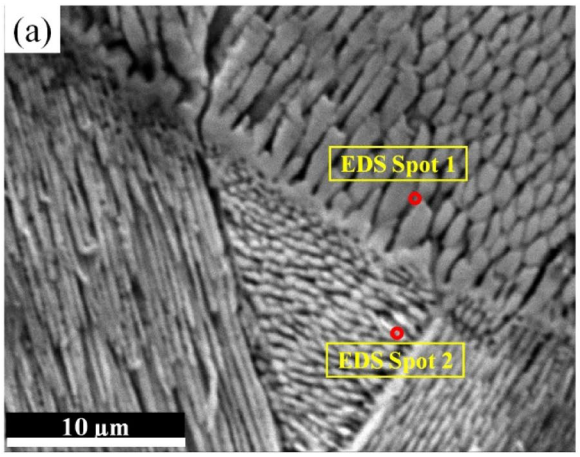

(b)

Element	Spot 1 (Weight %)	Spot 2 (Weight %)
Mo	6.76	3.53
Cr	15.20	16.88
Fe	66.01	66.69
Ni	9.51	9.32
Cu	2.51	3.58

Fig. 6 **a** Backscattered SEM image and **b** EDS elemental analysis of spot 1 and spot 2

and ε_f of the as-built AISI316L are 542 MPa, 500 MPa, and 25.6%. This discrepancy in the mechanical properties can be originated from the microstructural effects of copper that have been reported and discussed before. Generally, the solution strengthening of the Cu addition to the stainless steel would substantially increase the strength of AISI316L samples.

Table 2 summarises the average mechanical properties of the new stainless steel developed in this work together with those manufactured through conventional methods. The difference in the mechanical performance of these alloys might be due to the quantity of copper, fabrication method and post heat treatment of samples.

The fracture surface morphology of the as-built AISI316L and AISI316L-Cu samples after the tensile test at room temperature is shown in Fig. 8.

As can be seen, macro-scale necking could be observed in the fracture surfaces. Moreover, it is found that the ductile fracture surfaces of the as-built AISI316L, with and without Cu, are similar.

In-depth characterisation of the fracture surface shows ductile fracture with dimple networks, which explains the

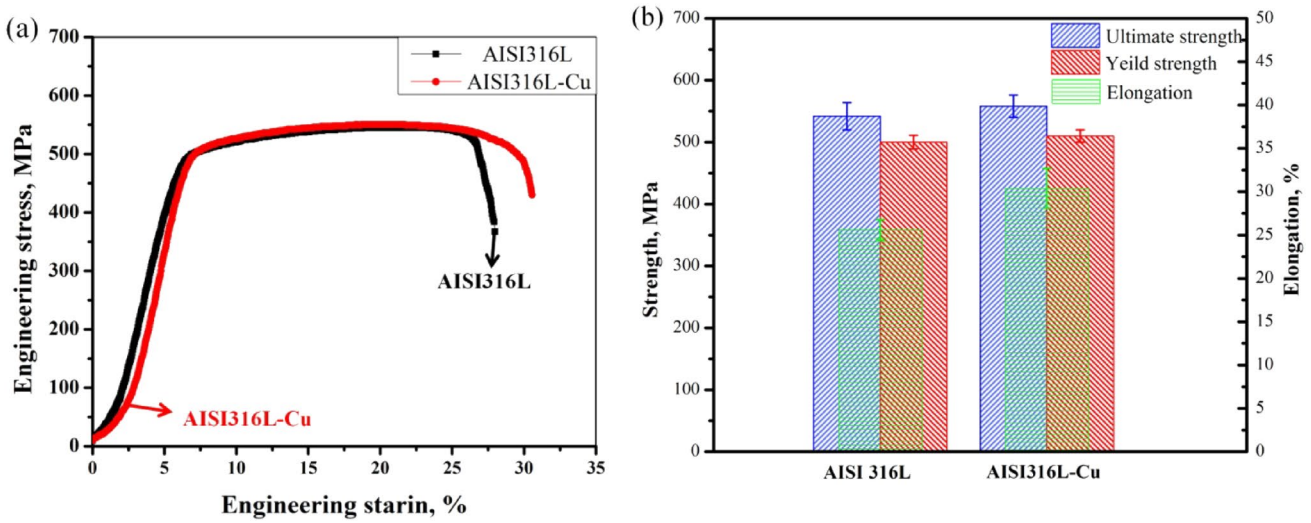

Fig. 7 **a** Engineering stress–strain curves and **b** results of tensile test of the as-built AISI316L and AISI316L-Cu samples

Table 2 A comparison of the present L-PBF AISI316L-Cu with literature in room temperature tensile properties

Samples	YS (MPa)	UTS (MPa)	Elongation to fracture (%)	Refs
AISI316L (L-PBF/as-built)	500 ± 14	542 ± 22	25.6 ± 1.2	Current work
AISI316L-2.5%Cu (L-PBF/as-built)	510 ± 10	558 ± 18	30.4 ± 2.3	Current work
AISI316L-1%Cu (L-PBF/as-built)	493	547	20.6	[24]
AISI316L-5%Cu (L-PBF/as-built)	476	536	12.8	[24]
AISI316-3.5% Cu (cast + solution)	229	507	54	[22]
AISI316-3.5% Cu (cast + solution + ageing)	257	543	60	[22]

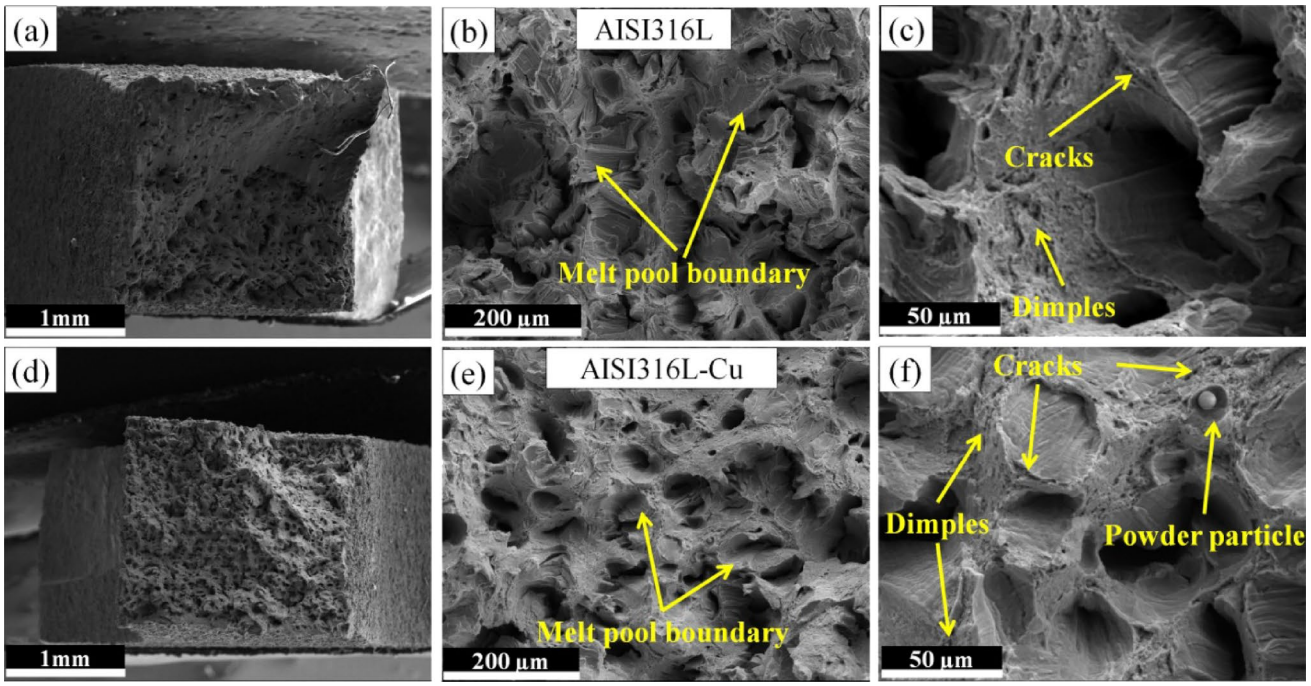

Fig. 8 Fracture surfaces of the **a–c** as-built AISI316L and **d–f** AISI316L-Cu samples

30% elongation of the as-built sample and brittle fracture with protrusions (Fig. 8b, e). A quasi-cleavage plane, which may indicate the melt pool boundary, is seen between the layered structures. The melt pool boundaries have insufficient interfacial bonding and are likely to be critical areas for the crack initiation and failure of the sample under the tensile stresses. However, many dimples of various sizes are noticed on the fracture surface of the samples. The size of dimples is usually in accordance with the extent of intragranular cells (Fig. 8c, f). As shown in Fig. 8f, an unmelted spherical particle of the powder and the cracks appeared near the melt boundaries during testing. It is proved that these particles can facilitate crack growth under tensile stresses. It is well reported that in the L-PBF process, partially melted and unmelted powder particles can remain in the area between melt pools and deteriorate the mechanical strength of the samples [12]. As a matter of fact, during the tensile test, those particles easily detach and form crater-like voids much larger than the typical dimple, which remain on the fracture surface. However, it should be mentioned that by optimising the processing parameters in the L-PBF process, it would be possible to minimise this defect content and improve the mechanical properties of the material significantly.

4 Conclusions

This paper has investigated the effect of the copper addition on the microstructure and mechanical properties of AISI316L samples produced via the L-PBF process. The following conclusions can be drawn:

1. According to the XRD analysis, the copper atom dissolves into iron, forming a complete austenitic structure under the L-PBF process.
2. Microstructural observations reveal that the columnar type of grains and fine cell structures formed along the building direction.
3. The comparison between the microstructure of the as-built AISI316L and AISI316L-Cu sample indicated that the formation of 0.77 µm and 0.68 µm cells resulted from a cooling rate equal to 1.1×10^6 K/s and 1.8×10^6 K/s, respectively.
4. The energy-dispersive X-ray spectroscopy maps verified that the distribution of copper in the AISI 316L samples was homogeneous, and no significant segregation of elements in the matrix was found.
5. The results of the tensile tests reveal that the copper addition, even in very low quantities, can alter the mechanical characteristics of the as-built AISI316L.

Funding Open access funding provided by Politecnico di Torino within the CRUI-CARE Agreement.

Data availability The data will be available upon a request.

References

1. Herzog D, Seyda V, Wycisk E, Emmelmann C (2016) Additive manufacturing of metals. Acta Mater. https://doi.org/10.1016/j.actamat.2016.07.019
2. Dadkhah M, Mosallanejad MH, Iuliano L, Saboori A (2021) A comprehensive overview on the latest progress in the additive manufacturing of metal matrix composites: potential, challenges, and feasible solutions. Acta Metall Sin (English Lett) 34:1173–1200. https://doi.org/10.1007/s40195-021-01249-7
3. Gao W, Zhang Y, Ramanujan D et al (2015) The status, challenges, and future of additive manufacturing in engineering. Comput Des 69:65–89. https://doi.org/10.1016/j.cad.2015.04.001
4. Mosallanejad MH, Niroumand B, Aversa A et al (2021) Laser powder bed fusion in-situ alloying of Ti-5%Cu alloy: process-structure relationships. J Alloys Compd 857:157558. https://doi.org/10.1016/j.jallcom.2020.157558
5. Sames WJ, List FA, Pannala S et al (2016) The metallurgy and processing science of metal additive manufacturing. Int Mater Rev 61:315–360. https://doi.org/10.1080/09506608.2015.1116649
6. Behjat A, Shamanian M, Taherizadeh A et al (2023) Microstructure-electrochemical behavior relationship in post processed AISI316L stainless steel parts fabricated by laser powder bed fusion. J Mater Res Technol 23:3294–3311. https://doi.org/10.1016/j.jmrt.2023.01.229
7. Sander G, Thomas S, Cruz V et al (2017) On the corrosion and metastable pitting characteristics of 316L stainless steel produced by selective laser melting. J Electrochem Soc 164:C250–C257. https://doi.org/10.1149/2.0551706jes
8. Saboori A, Toushekhah M, Aversa A et al (2020) Critical features in the microstructural analysis of AISI 316L produced by metal additive manufacturing. Metallogr Microstruct Anal 9:92–96. https://doi.org/10.1007/s13632-019-00604-6
9. Liu Y, Yang J, Yang H et al (2021) Cu-bearing 316L stainless steel coatings produced by laser melting deposition: microstructure and corrosion behavior in simulated body fluids. Surf Coatings Technol 428:127868. https://doi.org/10.1016/j.surfcoat.2021.127868
10. Hong IT, Koo CH (2005) Antibacterial properties, corrosion resistance and mechanical properties of Cu-modified SUS 304 stainless steel. Mater Sci Eng A 393:213–222. https://doi.org/10.1016/j.msea.2004.10.032
11. Saboori A, Aversa A, Marchese G et al (2020) Microstructure and mechanical properties of AISI 316L produced by directed energy deposition-based additive manufacturing: a review. Appl Sci. https://doi.org/10.3390/app10093310

12. Sohrabpoor H, Salarvand V, Lupoi R et al (2021) Microstructural and mechanical evaluation of post-processed SS 316L manufactured by laser-based powder bed fusion. J Mater Res Technol 12:210–220. https://doi.org/10.1016/J.JMRT.2021.02.090
13. Lodhi MJK, Deen KM, Greenlee-Wacker MC, Haider W (2019) Additively manufactured 316L stainless steel with improved corrosion resistance and biological response for biomedical applications. Addit Manuf 27:8–19. https://doi.org/10.1016/j.addma.2019.02.005
14. Wang Q, Ren L, Li X et al (2016) Antimicrobial Cu-bearing stainless steel scaffolds. Mater Sci Eng C 68:519–522. https://doi.org/10.1016/j.msec.2016.06.038
15. Mosallanejad MH, Niroumand B, Aversa A, Saboori A (2021) In-situ alloying in laser-based additive manufacturing processes: a critical review. J Alloys Compd 872:159567. https://doi.org/10.1016/j.jallcom.2021.159567
16. Vukkum VB, Gupta RK (2022) Review on corrosion performance of laser powder-bed fusion printed 316L stainless steel: effect of processing parameters, manufacturing defects, post-processing, feedstock, and microstructure. Mater Des 221:110874. https://doi.org/10.1016/j.matdes.2022.110874
17. Zhai W, Zhou W, Nai SML (2022) Grain refinement of 316L stainless steel through in-situ alloying with Ti in additive manufacturing. Mater Sci Eng A 840:142912. https://doi.org/10.1016/j.msea.2022.142912
18. Quan J, Lin K, Gu D (2020) Selective laser melting of silver submicron powder modified 316L stainless steel: influence of silver addition on microstructures and performances. Powder Technol 364:478–483. https://doi.org/10.1016/j.powtec.2020.01.082
19. Tanprayoon D, Srisawadi S, Sato Y et al (2020) Microstructure and hardness response of novel 316L stainless steel composite with TiN addition fabricated by SLM. Opt Laser Technol 129:106238. https://doi.org/10.1016/j.optlastec.2020.106238
20. Salman OO, Gammer C, Eckert J et al (2019) Selective laser melting of 316L stainless steel: influence of TiB2 addition on microstructure and mechanical properties. Mater Today Commun 21:100615. https://doi.org/10.1016/j.mtcomm.2019.100615
21. Vukkum VB, Christudasjustus J, Darwish AA et al (2022) Enhanced corrosion resistance of additively manufactured stainless steel by modification of feedstock. npj Mater Degrad 6:1–11. https://doi.org/10.1038/s41529-021-00215-z
22. Gonzalez B, Castro CS, Buono VT et al (2003) The influence of copper addition on the formability of AISI 304 stainless steel. Mater Sci Eng A 343:51–56. https://doi.org/10.1016/S0921-5093(02)00362-3
23. Xi T, Shahzad MB, Xu D et al (2017) Effect of copper addition on mechanical properties, corrosion resistance and antibacterial property of 316L stainless steel. Mater Sci Eng C 71:1079–1085. https://doi.org/10.1016/j.msec.2016.11.022
24. Foadian F, Kremer R, Post M et al (2023) Investigation of in-situ low copper alloying of 316L using the powder bed fusion process. Solids 4:156–165. https://doi.org/10.3390/solids4030010
25. Zhao H, Ding Y, Li J et al (2022) Corrosion resistance of laser melting deposited Cu-bearing 316L stainless steel coating in 0.5 M H 2 SO 4 solution. Mater Chem Phys 291:126572. https://doi.org/10.1016/j.matchemphys.2022.126572
26. Saboori A, Piscopo G, Lai M et al (2020) An investigation on the effect of deposition pattern on the microstructure, mechanical properties and residual stress of 316L produced by directed energy deposition. Mater Sci Eng A 780:139179. https://doi.org/10.1016/j.msea.2020.139179